Phonon contribution in grazing-incidence fast atom diffraction from insulator surfaces

L. Frisco and M. S. Gravielle*

Instituto de Astronomía y Física del Espacio (UBA-CONICET), Casilla de Correo 67, Sucursal 28, (C1428EGA) Buenos Aires, Argentina

(Received 25 September 2019; published 5 December 2019)

We study the effect of crystal lattice vibrations on grazing-incidence fast atom diffraction (GIFAD) from insulator surfaces. To describe the phonon contribution to GIFAD we introduce a semiquantum method named phonon-surface initial value representation (P-SIVR), which represents the surface with a harmonic-crystal model, while the scattering process is described by means of the surface initial value representation approach, including phonon excitations. Expressions for the partial scattering probabilities involving zero- and one-phonon exchange are derived. In particular, the P-SIVR approach for zero-phonon scattering is applied to study the influence of thermal lattice vibrations on GIFAD patterns for Ne/LiF(001) at room temperature. It is found that the thermal lattice fluctuations introduce a polar-angle spread into the projectile distributions, which can affect the relative intensities of the interference maxima, even giving rise to interference subpatterns depending on the incidence conditions. Present results are in agreement with the available experiments.

DOI: 10.1103/PhysRevA.100.062703

I. INTRODUCTION

Like in any interference phenomenon, in grazing-incidence fast atom diffraction (GIFAD or FAD) from ordered surfaces, the observation of interference patterns depends on the coherence conditions [1–3]. In this regard, since the early reports of GIFAD [4,5] thermal lattice vibrations were suspected of deteriorating the coherence, making the observation of interference structures completely unexpected [6,7]. This was based on the fact that in typical GIFAD experiments the de Broglie wavelengths of the projectiles are much smaller than the mean thermal fluctuations of the surface atoms, which would suggest a strong coherence loss. However, over the last decade GIFAD was observed for a wide variety of materials at room temperature [8–15], indicating that the quantum interference prevails over the decoherence mechanisms. Moreover, GIFAD patterns were found to be extremely sensitive to the projectile-surface interaction, allowing the determination of surface parameters smaller than the thermal vibration amplitudes, such as rumpling [16] or corrugation [17] distances.

From a theoretical point of view, in spite of the above-mentioned features, most of the GIFAD models [18–21] consider an ideal and static crystal surface, with atoms or ions at rest at their equilibrium positions. On the other hand, few articles deal with the decoherence introduced in GIFAD by lattice vibrations [6,7,16,22,23], so this issue represents a problem not fully understood yet.

In this paper we study the effect of lattice vibrations, i.e., phonons, on GIFAD distributions from insulator surfaces. This kind of surface is a good candidate to investigate the partial decoherence introduced by phonons, because the presence of a wide band gap strongly suppresses the electronic excitations of the target, causing the main source of decoherence to come from the vibrational movements of the surface atoms [24,25].

With a view to describe the collision with a realistic crystal that enables phonon transitions, we develop a semiquantum method named the phonon-surface initial value representation (P-SIVR) approximation. It is based on the previous SIVR approach for elastic scattering from a rigid surface [20], which was successfully employed to describe experimental GIFAD patterns for different collision systems [3,26–28]. The basic idea of the P-SIVR method is to incorporate a quantum representation of the surface, given by the harmonic-crystal model [29], making possible a description of the phonon effects involved in the GIFAD process.

Within the P-SIVR approximation, the scattering probability can be expressed as a series in terms of the number n of phonons emitted or absorbed during the collision. Each term of the series, named here the Pn-SIVR probability, is associated with the grazing scattering involving the exchange of n phonons. Mathematical formulas for the Pn-SIVR probabilities corresponding to $n = 0$ and $n = 1$ exchanged phonons are presented.

In this work the P0-SIVR approach for zero-phonon scattering is applied to study the influence of thermal lattice vibrations on GIFAD patterns for Ne/LiF(001) at room temperature. With the aim of examining the thermal contribution, P0-SIVR results for different incidence conditions are compared with values derived from the SIVR approach for the static surface. In all the considered cases, it is found that the thermal lattice vibrations contribute to the polar-angle spread of the projectile distributions, in accord with previous predictions [7]. Furthermore, depending on the incidence conditions, such thermal fluctuations can affect the relative intensity of the interference peaks, even introducing an interference subpattern, as it is observed at a high normal energy. We show that present P0-SIVR results are in very good agreement with the available experimental data [30]. In addition, results from an incoherent model to include thermal lattice vibrations are analyzed.

*Author to whom correspondence should be addressed: msilvia@iafe.uba.ar

The article is organized as follows. The P-SIVR approach is summarized in Sec. II, while details about its derivation are given in the Appendix. Results are presented and discussed in Sec. III, and in Sec. IV we outline our conclusions. Atomic units (a.u.) are used unless otherwise stated.

II. THEORETICAL MODEL

The P-SIVR approximation can be considered as a natural extension of the SIVR approach [20] to incorporate phonon effects into the GIFAD description. Summarizing, within the P-SIVR approximation the atom-surface scattering probability corresponding to the transition $\mathbf{K}_i \to \mathbf{K}_f$, with $\mathbf{K}_i$ ($\mathbf{K}_f$) being the initial (final) projectile momentum, is evaluated by adding the partial contributions coming from the different initial and final crystal states, which are derived from a quantum harmonic-crystal model [29]. The result is then expanded in terms of the number n of phonons that are exchanged with the crystal, giving rise to a series of Pn -SIVR probabilities associated with n-phonon scattering. In this section we present mathematical expressions of the Pn-SIVR probability for $n = 0$ and $n = 1$, while the general formula for a given value of n, as well as the steps involved in its derivation, are given in the Appendix.

The P0-SIVR probability for the transition $\mathbf{K}_i \to \mathbf{K}_f$ without phonon exchange, which corresponds to the elastic scattering with $K_f = K_i$, can be expressed as

$$\frac{dP_0}{d\mathbf{K}_f} = \left|\mathcal{A}_{n_{\rm ph}=0}\right|^2, \tag{1}$$

while the P1-SIVR probability for one-phonon scattering reads

$$\frac{dP_1}{d\mathbf{K}_f} = \sum_{\mathbf{k},l}\left[\frac{N_l(\mathbf{k})}{\omega_l(\mathbf{k})}\left|\mathcal{A}_{n_{\rm ph}=-1}(\mathbf{k},l)\right|^2 + \frac{N_l(\mathbf{k})+1}{\omega_l(\mathbf{k})}\left|\mathcal{A}_{n_{\rm ph}=+1}(\mathbf{k},l)\right|^2\right], \tag{2}$$

where $\mathcal{A}_{n_{\rm ph}}$ is the effective transition amplitude for scattering involving $n_{\rm ph} = \pm n$ phonons emitted ($n_{\rm ph} = -n$) or absorbed ($n_{\rm ph} = +n$) by the crystal. In Eq. (2) the sum runs over all the normal modes of the crystal, with $\omega_l(\mathbf{k})$ being the phonon frequency in the branch l, with the wave vector $\mathbf{k}$. The factor $N_l(\mathbf{k}) = (\exp[\omega_l(\mathbf{k})/(k_B T)] - 1)^{-1}$ is the Bose-Einstein occupation function for $(\mathbf{k}, l)$ phonons in a crystal target at temperature T, with k_B being the Boltzmann constant.

In Eqs. (1) and (2), the effective transition amplitude $\mathcal{A}_{n_{\rm ph}}(\mathbf{k}, l)$ reads

$$\mathcal{A}_{n_{\rm ph}}(\mathbf{k},l) = \int d\mathbf{R}_o\, f(\mathbf{R}_o)\int d\mathbf{K}_o\, g(\mathbf{K}_o) \times \int d\underline{\mathbf{u}}_o\, a^{(\mathbf{k},l)}_{n_{\rm ph}}(\mathbf{R}_o,\mathbf{K}_o,\underline{\mathbf{u}}_o), \tag{3}$$

where the function f (g) describes the position (momentum) profile of the incident wave packet and

$$a^{(\mathbf{k},l)}_{n_{\rm ph}}(\mathbf{R}_o,\mathbf{K}_o,\underline{\mathbf{u}}_o) = \int_0^{+\infty} dt\; |J_P(t)|^{1/2} e^{i\nu_t \pi/2}\, \mathcal{V}^{(\mathbf{k},l)}_n(\mathbf{R}_t) \times \exp[i(\varphi_t - \mathbf{Q}\cdot\mathbf{R}_o + n_{\rm ph}\omega_l(\mathbf{k})t)] \tag{4}$$

represents the partial amplitude associated with the classical projectile trajectory $\mathbf{R}_t \equiv \mathbf{R}_t(\mathbf{R}_o, \mathbf{K}_o, \underline{\mathbf{u}}_o)$, which starts at the position $\mathbf{R}_o$ with momentum $\mathbf{K}_o$ and is determined by the spatial configuration $\underline{\mathbf{u}}_o$ of the crystal at the initial time $t = 0$. That is, the underlined vector $\underline{\mathbf{u}}_o$ denotes the $3N$-dimension vector associated with the spatial deviations of the N ions contained in the crystal sample, with respect to their equilibrium positions, at $t = 0$ [29].

In Eq. (4), $J_P(t) = |J_P(t)|\exp(i\nu_t\pi)$ is the Jacobian factor given by Eq. (A10), φ_t is the SIVR phase at the time t [Eq. (A14)], and $\mathbf{Q} = \mathbf{K}_f - \mathbf{K}_i$ is the projectile momentum transfer. The function $\mathcal{V}^{(\mathbf{k},l)}_n(\mathbf{R}_t)$ is a crystal factor that depends on the number n of exchanged phonons. For zero-phonon scattering, $\mathcal{V}^{(\mathbf{k},l)}_0(\mathbf{R}_t)$ is independent of $(\mathbf{k}, l)$ and can be expressed as

$$\mathcal{V}_0(\mathbf{R}_t) = \int d\mathbf{q} \sum_{\mathbf{r}_{\rm B}} \tilde{v}_{\mathbf{r}_{\rm B}}(\mathbf{q})\exp\big[-W_{\mathbf{r}_{\rm B}}(\mathbf{q})\big] \times \exp[i\mathbf{q}\cdot(\mathbf{R}_t - \mathbf{r}_{\rm B})], \tag{5}$$

where $\tilde{v}_{\mathbf{r}_{\rm B}}(\mathbf{q})$ denotes the Fourier transform of the binary interaction between the projectile and the crystal ion placed at the Bravais position $\mathbf{r}_{\rm B}$, with $v_{\mathbf{r}_{\rm B}}$ coming from Eq. (A16). The summation on $\mathbf{r}_{\rm B}$ covers all the occupied lattice sites, and $W_{\mathbf{r}_{\rm B}}(\mathbf{q})$ is the usual momentum-dependent Debye-Waller function, defined by Eq. (A21).

For one-phonon scattering, instead, $\mathcal{V}^{(\mathbf{k},l)}_1(\mathbf{R}_t)$ depends on $(\mathbf{k}, l)$, reading

$$\mathcal{V}^{(\mathbf{k},l)}_1(\mathbf{R}_t) = \int d\mathbf{q}\,[\mathbf{q}\cdot\alpha_l(\mathbf{k})]\sum_{\mathbf{r}_{\rm B}} \tilde{v}_{\mathbf{r}_{\rm B}}(\mathbf{q})\exp\big[-W_{\mathbf{r}_{\rm B}}(\mathbf{q})\big] \times \exp[i\mathbf{q}\cdot\mathbf{R}_t + i(\mathbf{k}-\mathbf{q})\cdot\mathbf{r}_{\rm B}], \tag{6}$$

where $\alpha_l(\mathbf{k})$ is the polarization vector corresponding to the $(\mathbf{k}, l)$ phonon.

From Eq. (5) it can be noted that in the absence of the Debye-Waller factor, $\exp[-W_{\mathbf{r}_{\rm B}}(\mathbf{q})]$, $\mathcal{V}_0(\mathbf{R}_t)$ coincides with the projectile-surface potential for an ideal crystal, given by Eq. (A16) with $\underline{\mathbf{u}} = 0$. Therefore, within the P0-SIVR approach the contribution of the thermal lattice vibrations can be seen as an effective screening of the projectile-surface interaction, given by the Debye-Waller factor, in addition to the thermal effect on the projectile trajectories that is produced by the different crystal configurations $\underline{\mathbf{u}}_o$.

III. RESULTS

In this article we investigate the influence of the thermal lattice vibrations on GIFAD patterns produced by ^{20}Ne atoms grazingly colliding with a LiF(001) surface at room temperature. Incidence along the ⟨110⟩ direction, for which experimental spectra were reported [30], is analyzed. Concerning the atomic projectile, the relatively large mass of neon is expected to play some role in inelastic processes such as phonon excitations [23,24]. However, we confine our study to the P0-SIVR approach, corresponding to zero-phonon scattering, leaving the investigation of one-phonon excitations, as given by Eq. (2), for a future work.

The P0-SIVR probability for scattering in the direction of the solid angle $\Omega_f = (\theta_f, \varphi_f)$ was derived from Eq. (1) as

$$dP_0/d\Omega_f = K_f^2 \left|\mathcal{A}_{n_{\rm ph}=0}\right|^2, \tag{7}$$

where θ_f is the final polar angle, measured with respect to the surface, and φ_f is the azimuthal angle, measured with respect to the axial channel. The transition amplitude $\mathcal{A}_{n_{\rm ph}=0}$ was calculated from Eq. (3), where the integration on $\mathbf{R}_o$ was reduced to the plane parallel to the surface, $\mathbf{R}_{o\parallel}$, by considering that at $t = 0$ all classical trajectories start at a fixed distance Z_o from the surface, chosen as equal to the lattice constant, for which the projectile is hardly affected by the surface interaction [3,20]. In turn, the integral on $\mathbf{K}_o$ was solved in terms of the solid angle $\Omega_o = (\theta_o, \varphi_o)$ that determines the $\mathbf{K}_o$ orientation, with $K_o = K_i$ accounting for the negligible energy dispersion of the incident beam [2,3]. In Eq. (3), the wave-packet profiles $f(\mathbf{R}_{o\parallel})$ and $g(\Omega_o)$ were represented by products of Gaussian functions as respectively given by Eqs. (12) and (14) of Ref. [3]. The widths of these profiles depend on the collimating setup and the incidence conditions [3,31]. However, in this work we have used fixed values for such dispersion widths in order to control their influence on the GIFAD patterns. Specifically, in Secs. III A and III B the angular widths were chosen as $\Delta\theta_o = \Delta\varphi_o = 0.03$ deg, values that are in the range of the experimental conditions [30].

The projectile-surface interaction was described with the pairwise additive model of Ref. [32]. In addition, the integral on $\underline{\mathbf{u}}_o$ involved in Eq. (3) was evaluated by considering that each crystal ion is randomly displaced from its equilibrium position following an independent Gaussian distribution, with a mean-square vibrational amplitude $\langle \mathbf{u}(\mathbf{r}_{\rm B})^2 \rangle$. For the LiF(001) target at temperature $T = 300$ K, the $\langle \mathbf{u}(\mathbf{r}_{\rm B})^2 \rangle$ values were extracted from Ref. [16] by taking into account the differences between Li and F ions and between bulk and surface (topmost layer) sites. Note that while in Ref. [16] thermal effects were included as an additional negative corrugation of the atom-surface potential, derived by averaging the interaction potential over randomly displaced positions of the crystal ions, within the P-SIVR approach such displaced ion positions participate in the projectile dynamics as well as in the effective screening of the potential along the projectile path, as given by the Debye-Waller factor in Eq. (5).

For the calculation of $\mathcal{V}_0(\mathbf{R}_t)$ [Eq. (5)], the Debye-Waller function was approximated as $W_{\mathbf{r}_{\rm B}}(q) \simeq q^2 \langle \mathbf{u}(\mathbf{r}_{\rm B})^2 \rangle / 2$ [22,29]. This assumption allowed us to transform the $\mathbf{q}$-integral involved in Eq. (5) into a space integral, which was solved together with the $\mathbf{R}_{o\parallel}$, Ω_o, and $\underline{\mathbf{u}}_o$ integrals of Eq. (3) by employing the Monte Carlo technique, with more than 6×10^6 points for each incidence condition. Furthermore, for each integration point the time integral involved in Eq. (4) was numerically solved by using an adaptive-stepsize method, with an error lower than 1%. In this respect, the incorporation of $\underline{\mathbf{u}}_o$ into the evaluation of the projectile trajectories leads to strongly increase the numerical effort necessary to reach the convergency of the Monte Carlo integration, in relation to that required within the SIVR approach [20].

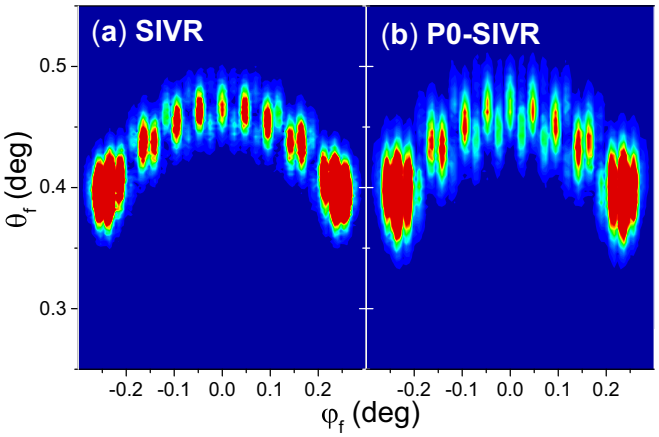

FIG. 1. Two-dimensional projectile distributions as a function of θ_f and φ_f for Ne atoms impinging on LiF(001) along the ⟨110⟩ channel, with $E = 3.0$ keV and $\theta_i = 0.47$ deg. Results derived within (a) the SIVR approximation for a static crystal and (b) the P_0-SIVR approach, including thermal vibrations, are displayed.

A. Thermal influence on GIFAD patterns

In Fig. 1 we show SIVR and P0-SIVR two-dimensional (2D) distributions as a function of the final angles θ_f and φ_f, for Ne atoms impinging with the kinetic energy $E = K_i^2/(2m_P) = 3.0$ keV, m_P being the projectile mass, and the incidence angle $\theta_i = 0.47$ deg, measured with respect to the surface plane. Results for zero-phonon scattering derived within the P0-SIVR approximation, displayed in the right panel of Fig. 1, include the phonon contribution, while the SIVR distribution, shown in the left panel, was obtained by considering a static LiF crystal, with its ions at rest at their equilibrium positions [20]. Within both approaches, the width of the spatial profile $f(\mathbf{R}_{o\parallel})$ was chosen to cover two equivalent parallel channels, which gives rise to Bragg maxima produced by interchannel interference [3].

In Figs. 1(a) and 1(b) the Bragg maxima look like vertical strips placed inside an annulus with mean radius θ_i due to the energy conservation. Even though the SIVR and P0-SIVR distributions of Fig. 1 display qualitatively similar interference patterns, with almost the same φ_f extension of the spectrum, the relative intensities of the interference maxima, as well as the θ_f angular spreads, predicted by the two approximations differ from each other, these discrepancies being indicative of the effect of the thermal lattice vibrations.

To look with more detail into the projectile distributions of Fig. 1, in Fig. 2 we plot the corresponding $dP_0/d\Theta_f$ probabilities as a function of the deflection angle $\Theta_f = \arctan(\varphi_f/\theta_f)$. These differential probabilities were obtained by integrating Eq. (7) over a reduced annulus of mean radius θ_i and central thickness 0.03 deg, as it is usually done to derive the experimental projected intensities [33,34]. From Fig. 2 we observe that the angular positions of the Bragg peaks (indicated with vertical lines in the inset) are not affected by the thermal vibrations, coinciding for the P0-SIVR and SIVR approximations. Instead, the relative intensities of the Bragg maxima are strongly modified by the contribution of the thermal fluctuations included in the P0-SIVR approach, which can increase or reduce the SIVR intensity of a given

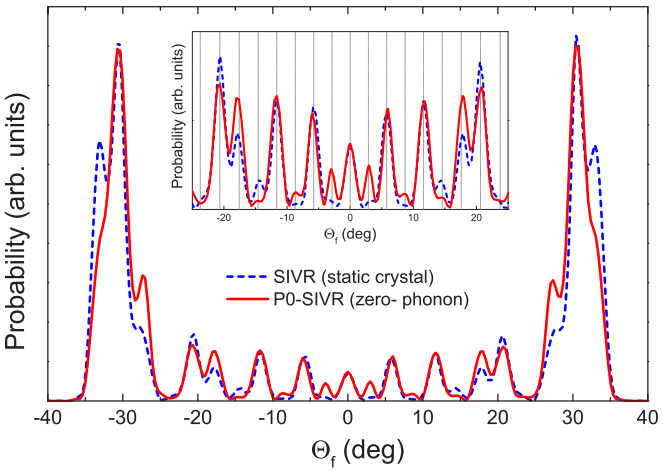

FIG. 2. Differential probability as a function of the deflection angle Θ_f for the case of Fig. 1. Red solid line, zero-phonon scattering probability derived within the P_0-SIVR approach; blue dashed line, SIVR probability for a static crystal. The inset displays a zoomed view of the central region of the spectrum. Dashed vertical lines indicate Bragg-peak positions.

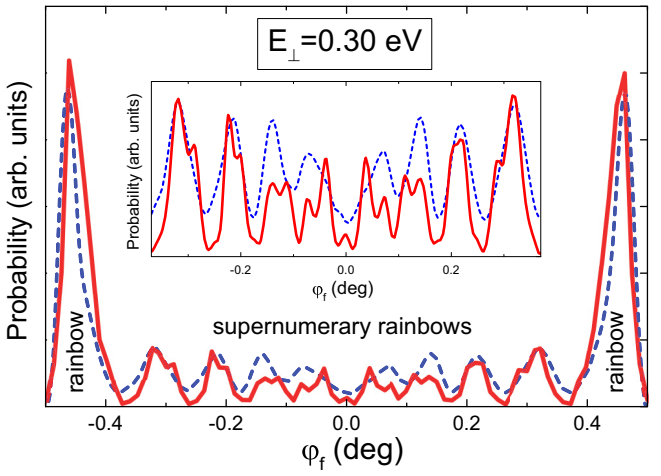

FIG. 3. Intrachannel distribution as a function of the final azimuthal angle φ_f for $E = 1.3$ keV and the normal energy $E_\perp = 0.30$ eV. Lines analogous to Fig. 2. Inset: Zoomed view of the central region.

Bragg order, as shown in the inset of Fig. 2. Hence, since the use of GIFAD for surface analysis is commonly based on the comparison of the relative intensities of the interference maxima with theoretical models, these results suggest that the thermal vibrations might play an important role in the GIFAD technique.

At this point, it is important to take into account that the Bragg-peak intensities are determined by an intrachannel factor due to the interference inside a single channel, which acts as an enveloped function of the interchannel interference [20]. Therefore, for the purpose of analyzing the influence of lattice vibrations on the Bragg intensities under different incidence conditions, hereinafter we restrict our study to pure intrachannel spectra, which are produced by initial wave-packet profiles covering a transverse distance equal to the channel width [31].

B. Thermal effects in the intrachannel interference

GIFAD distributions due to a single coherently illuminated channel are governed by the normal incidence energy, $E_\perp = E \sin^2\theta_i$, which is associated with the projectile motion perpendicular to the surface plane [33,35]. In Fig. 3 we display P0-SIVR and SIVR intrachannel spectra as a function of the azimuthal angle φ_f, for $E = 1.3$ keV and $E_\perp = 0.30$ eV. Notice that this normal energy is barely lower than the upper $E_\perp$ limit of available GIFAD experiments for Ne/LiF(001) [30]. Both curves of Fig. 3 display equivalent interference patterns, with rainbow and supernumerary rainbow maxima. While the rainbow peaks corresponding to the high-intensity outermost maxima have a classical origin, the supernumerary peaks are produced by quantum interference, being expected to be more affected by thermal fluctuations than the rainbow, which is confirmed in Fig. 3.

The P0-SIVR spectrum of Fig. 3 presents a small angular shift in the positions of the central supernumeraries with respect to those corresponding to the SIVR curve. But in addition, it is observed that the thermal vibrations included in the P0-SIVR approach affect the shape and relative intensity of the supernumerary peaks, especially in the central region of the spectrum where a noticeable double-peak structure is clearly visible in each supernumerary maxima (see the inset of Fig. 3). Remarkably, this interference subpattern that appears as a superimposed structure on the P0-SIVR supernumeraries is mainly produced by the effect of the thermal deviations $\underline{\mathbf{u}}_o$ on the projectile trajectories. When the $\mathbf{R}_t$ dependence on $\underline{\mathbf{u}}_o$ is left aside, results derived from Eq. (1) by considering an ideal and static crystal, but keeping the factor $\exp[-W_{\mathbf{r}_B}(\mathbf{q})]$ in Eq. (5), fully agree with the SIVR values, indicating that the Debye-Waller factor plays a minor role in the elastic scattering at room temperature.

To understand the origin of the interference subpatterns observed in Fig. 3, the corresponding 2D angular distributions, as a function of θ_f and φ_f, are plotted in Fig. 4. In Fig. 4(a) the SIVR distribution for the static crystal displays broad interference maxima, which lay on an annulus whose thickness

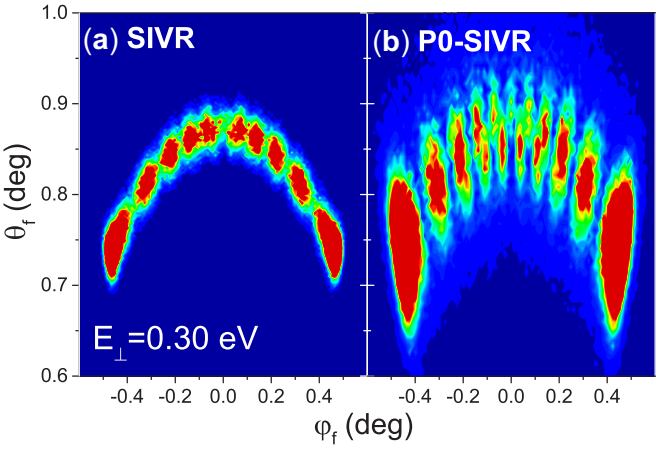

FIG. 4. Analogous to Fig. 1 for the case of Fig. 3, i.e., $E = 1.3$ keV and $E_\perp = 0.30$ eV.

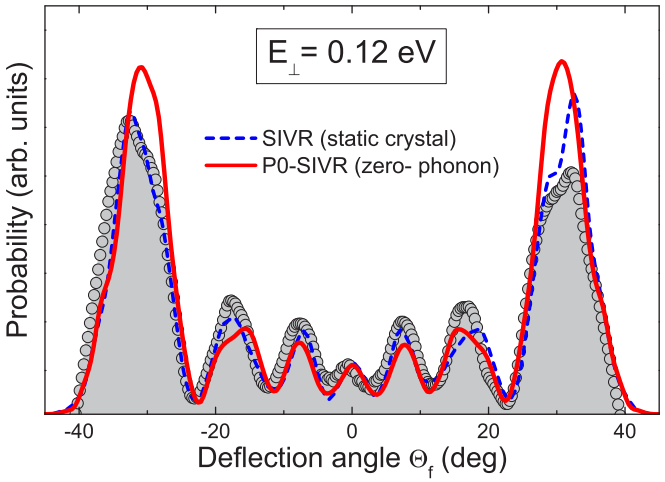

FIG. 5. Angular distribution as a function of the deflection angle Θ_f for the incidence energy $E = 1.3$ keV and angle $\theta_i = 0.55$ deg, i.e., $E_\perp = 0.12$ eV. Lines, analogous to Fig. 2; gray solid circles, experimental data from Ref. [30].

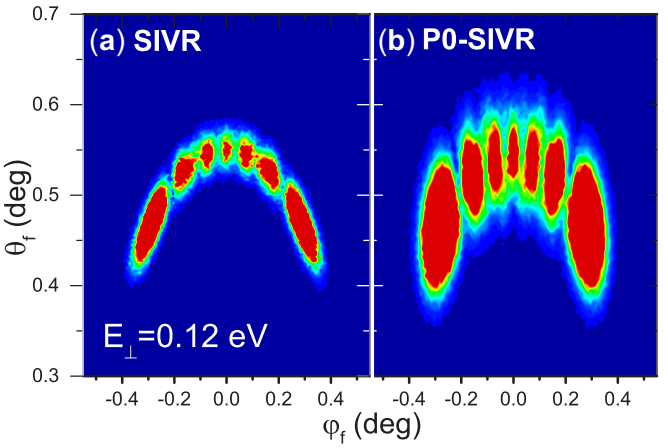

FIG. 6. Analogous to Fig. 1 for the case of Fig. 5, i.e., $E = 1.3$ keV and $E_\perp = 0.12$ eV.

is essentially determined by the polar-angle dispersion $\Delta\theta_o$ of the atomic beam [3,36]. Instead, in Fig. 4(b) the thermal lattice vibrations introduce an additional polar-angle spread into the P0-SIVR distribution, transforming the SIVR interference spots into vertical strips. The emergence of a polar-angle broadening as a consequence of thermal fluctuations was already proposed in Ref. [7]. Furthermore, it is found that the thermal vibrations give rise to an interference structure in the P0-SIVR distribution along θ_f, which is more evident around $\varphi_f \approx 0$. Then the double-peak shape of the internal P0-SIVR maxima of Fig. 3 corresponds to the projected image on φ_f of such a vertical pattern [7], which is produced by the interference among projectiles running nearly on top of thermally shifted Li and F rows [16].

C. Experimental comparison

In order to test the reliability of the proposed model, in Fig. 5 we contrast P0-SIVR and SIVR differential probabilities as a function of the deflection angle Θ_f, with the available experimental spectrum [30] for the incidence conditions $E = 1.3$ keV and $\theta_i = 0.55$ deg, which correspond to the normal energy $E_\perp = 0.12$ eV. Like in the previous section, in this case the theoretical and experimental distributions display only supernumerary peaks associated with intrachannel interference, without any trace of Bragg interference.

In Fig. 5, the P0-SIVR spectrum is very similar to that for a static crystal derived by means of the SIVR approach, both showing a very good agreement with the experimental data. This behavior, together with the absence of interference substructures in the P0-SIVR supernumeraries, might indicate that the thermal contribution on GIFAD patterns becomes smaller as $E_\perp$ decreases, since the atomic projectiles move farther from the surface plane.

However, notice that the Θ_f spectra displayed in Fig. 5 were also obtained by integrating the corresponding 2D angular distributions, shown in Fig. 6, inside an annulus of central thickness 0.03 deg [30,34]. When the distributions of Figs. 6(a) and 6(b) are compared, it is found that even though for this low perpendicular energy there are no visible signatures of interference substructures, the thermal motion of the crystal ions still introduces a wide polar-angle dispersion in the P0-SIVR distribution. It gives rise to a P0-SIVR pattern formed by elongated vertical streaks instead of the nearly circular spots of the SIVR distribution, a feature that it is also observed in the experimental data of Fig. 1(a) of Ref. [30]. By quantitatively contrasting this experimental distribution with that displayed in Fig. 6(b) we determine that the thermal effects included in the P0-SIVR approximation can explain about 60% of the experimental polar-angle spread. This suggests that there might be further mechanisms contributing to the θ_f dispersion of the GIFAD patterns, such as inelastic processes involving phonon transitions or the presence of crystal defects. Also, the collimating conditions of the atomic beam affect the polar-angle distribution, whose extension depends on the length of the collimating slit [3,36].

D. Incoherent thermal vibrations

Lastly, we investigate the role of the coherent thermal contribution involved in the present approach by comparing the P0-SIVR results with thermally incoherent probabilities derived from the SIVR approach. Such an incoherent calculation was done by averaging the SIVR probability, i.e., the square modulus of the SIVR transition amplitude [20], for different configurations $\underline{\mathbf{u}}_o$ of the crystal target, where the crystal ions are randomly displaced from their equilibrium positions following Gaussian distributions, as considered within the P0-SIVR model. In Fig. 7 we plot the thermally incoherent SIVR distribution as a function of θ_f and φ_f for the case of Fig. 4 corresponding to the normal energy $E_\perp = 0.30$ eV. By contrasting Figs. 4(b) and 7 we found that the incoherent addition of thermal effects destroys the interference subpattern observed in the central region of the P0-SIVR distribution of Fig. 4(b). Moreover, the thermally incoherent approach introduces a significant broadening of the supernumerary maxima along φ_f, while the θ_f dispersion is similar to that displayed by the P0-SIVR distribution. Although there is no available experimental distribution for

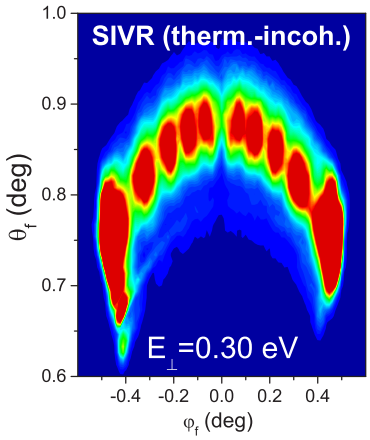

FIG. 7. Two-dimensional projectile distribution as a function of θ_f and φ_f evaluated with the thermally incoherent SIVR model, as explained in the text. Results for the case of Fig. 4, corresponding to $E_\perp = 0.30$ eV, are displayed.

this case, an analogous calculation for the case of Fig. 6 shows that this noticeable φ_f widening of the interference peaks associated with the incoherent thermal contribution does not agree with the reported experiments [30]. Therefore, the thermally incoherent SIVR approximation [32] seems to be unsuitable to reproduce thermal effects on GIFAD patterns.

IV. CONCLUSIONS

We have developed the P-SIVR approximation, which is a semiquantum method that takes into account the contribution of the vibrational modes of the crystal to the GIFAD patterns. The P-SIVR probability was expressed as a sum of partial scattering probabilities, Pn-SIVR, each of them involving the exchange of a different number n of phonons. Formulas for the probabilities corresponding to zero- and one-phonon scattering have been presented.

The P0-SIVR approach for zero-phonon scattering was employed to investigate the effect of thermal lattice vibrations on GIFAD distributions for the Ne/LiF(001) system. At room temperature it was found that, depending on the incidence conditions, the relative intensities of the Bragg peaks can be affected by the thermal fluctuations of the LiF(001) crystal. Within the P0-SIVR model, the thermal vibrations introduce a polar-angle dispersion into the angular distributions which contribute to transform the interference spots into elongated structures, in concordance with the experimental observations [30]. For high normal energies, such a polar-angle spread can also alter the shape of the supernumerary maxima, giving rise to the appearance of interference subpatterns in the central region of the GIFAD spectra.

In conclusion, the present P0-SIVR results demonstrate that thermal vibrations affect the aspect of the GIFAD patterns from insulator surfaces, a finding that is especially relevant for the use of GIFAD as a surface analysis technique. But notice that there are other effects, such as phonon excitations [22,23] or the presence of terraces in the crystal sample [37], not considered in this article which can modify the interference structures too. Therefore, further experimental and theoretical work to investigate the different decoherence mechanisms in GIFAD would be valuable.

ACKNOWLEDGMENTS

The authors acknowledge financial support from CONICET (PIP 2014- 11220130100386CO) and ANPCyT (PICT-2017-1201 and PICT-2017-2945) of Argentina.

APPENDIX: P-SIVR MODEL FOR GRAZING ATOM-SURFACE SCATTERING WITH PHONON EXCHANGE

In this Appendix we explain the steps and assumptions that lead to the P-SIVR approximation for GIFAD from an insulator target. Let us consider an atomic projectile (P), with initial momentum $\mathbf{K}_i$, which is scattered from a crystal surface (S), ending in a final state with momentum $\mathbf{K}_f$. The scattering state of the projectile-surface system at time t, $|\Psi_i(t)\rangle$, is governed by the time-dependent Schrödinger equation:

$$\left[\frac{\mathbf{P}_P^2}{2m_P} + H_S + V_{\rm PS}\right]|\Psi_i(t)\rangle = i\frac{d}{dt}|\Psi_i(t)\rangle, \qquad \text{(A1)}$$

where $\mathbf{P}_P$ denotes the momentum operator of the projectile with mass m_P, H_S is the unperturbed surface Hamiltonian, and $V_{\rm PS}$ is the perturbation produced by the projectile-surface interaction. The Hamiltonian H_S reads

$$H_S = \sum_{\mathbf{r}_B} \frac{\mathbf{P}^2(\mathbf{r}_B)}{2m(\mathbf{r}_B)} + \mathcal{W}_S(\underline{\mathbf{u}}), \qquad \text{(A2)}$$

where the sum runs over the positions $\mathbf{r}_B$ of the occupied Bravais lattice sites. In Eq. (A2) $\mathbf{P}(\mathbf{r}_B)$ indicates the momentum operator of the crystal ion that oscillates about $\mathbf{r}_B$ and $m(\mathbf{r}_B)$ is its mass, with $m(\mathbf{r}_B) = m_1$ or m_2 to include two different ions in the crystallographic basis. The potential $\mathcal{W}_S(\underline{\mathbf{u}})$ represents the potential energy of the crystal as a function of the multidimensional vector $\underline{\mathbf{u}}$, which is determined by the spatial deviations $\mathbf{u}(\mathbf{r}_B)$ of the crystal ions from their equilibrium positions $\mathbf{r}_B$, for all the occupied lattice sites [29].

As the initial condition, at $t = 0$, when the projectile is far away from the surface, the scattering state $|\Psi_i(t)\rangle$ tends to the state $|\chi_i(0)\rangle$, where

$$\chi_j(t) = e^{i\mathbf{K}_j\cdot\mathbf{R}_P}\phi_j(\underline{\mathbf{u}})\exp(-iE_jt), \quad j = i(f) \qquad \text{(A3)}$$

is the initial (final) unperturbed wave function with total energy

$$E_j = K_j^2/(2m_P) + \epsilon_j, \quad j = i(f), \qquad \text{(A4)}$$

which satisfies the energy conservation, i.e., $E_i = E_f$. In Eq. (A3), $\mathbf{R}_P$ is the position vector of the center of mass of the incident atom, and the wave function $\phi_j(\underline{\mathbf{u}})$, for $j = i(f)$, is the initial (final) eigenstate of H_S with eigenvalue ϵ_j.

By considering that the surface behaves like a harmonic crystal, H_S can be expressed as a sum of independent harmonic-oscillator Hamiltonians, each of them corresponding to a different normal mode of the lattice, with wave vector $\mathbf{k}$, frequency $\omega_l(\mathbf{k})$, and l denoting the phonon branch. Hence, the unperturbed crystal state ϕ_j for $j = i, f$ is determined by the excitation numbers $n^{(j)}_{\mathbf{k},l}$ of the normal modes, and the

corresponding crystal energy reads

$$\epsilon_j = \sum_{\mathbf{k},l} \omega_l(\mathbf{k}) \left[n^{(j)}_{\mathbf{k},l} + \frac{1}{2} \right], \quad j = i, f, \tag{A5}$$

where the sum runs over all the $(\mathbf{k}, l)$ normal modes of the crystal [29].

1. P-SIVR scattering state

Within the P-SIVR method, the scattering state $|\Psi_i(t)\rangle$ is approximated by means of the IVR method [38]. It is expressed as

$$\begin{aligned} \left|\Psi_i^{(\mathrm{P-SIVR})}(t)\right\rangle = & \int d\mathbf{R}_o \, f(\mathbf{R}_o) \int d\mathbf{K}_o \, g(\mathbf{K}_o) \\ & \times \int d\underline{\mathbf{u}}_o \int d\underline{\mathbf{p}}_o [J(t)]^{1/2} \exp(i\mathbf{K}_i \cdot \mathbf{R}_o) \\ & \times \exp(iS_t) \phi_i(\underline{\mathbf{u}}_o) |\mathbf{R}_t\rangle \otimes \left|\underline{\mathbf{u}}_t\right\rangle, \end{aligned} \tag{A6}$$

where the position ket $|\mathbf{R}_t\rangle$ is associated with the time-evolved position $\mathbf{R}_t$ of the incident atom at a given time t, which is derived by considering a classical trajectory with starting position and momentum $\mathbf{R}_o$ and $\mathbf{K}_o$, respectively. In a similar way, the deviation ket $|\underline{\mathbf{u}}_t\rangle$ is determined from the classical deviations $\mathbf{u}_t(\mathbf{r}_\mathrm{B})$ of all the crystal ions, starting at $t = 0$ from initial deviations and momenta $\mathbf{u}_o(\mathbf{r}_\mathrm{B})$ and $\mathbf{p}_o(\mathbf{r}_\mathrm{B})$, respectively. In Eq. (A6), $\underline{\mathbf{u}}_o$ ($\underline{\mathbf{p}}_o$) denotes the $3N$-dimension vector determined by such deviations (momenta) for the N ions contained in the crystal target. In fact, note that we are dealing with a many-particle problem in which the classical motions of the projectile and the crystal ions are related through their mutual interactions. Consequently, the classical trajectories $\mathbf{R}_t$ and $\mathbf{u}_t(\mathbf{r}_\mathrm{B})$, for the different $\mathbf{r}_\mathrm{B}$ values, depend on the initial positions and momenta of all the particles in the system.

Furthermore, in Eq. (A6) the functions $f(\mathbf{R}_o)$ and $g(\mathbf{K}_o)$ describe the shape of the position and momentum wave packet associated with the incident projectile, while S_t represents the classical action along the trajectory, reading

$$\begin{aligned} S_t = \int_0^t dt' \Bigg[& \frac{\mathbf{K}_{t'}^2}{2m_P} - V_\mathrm{PS}(\mathbf{R}_{t'}, \underline{\mathbf{u}}_{t'}) \\ & + \sum_{\mathbf{r}_\mathrm{B}} \frac{\mathbf{p}_{t'}^2(\mathbf{r}_\mathrm{B})}{2m(\mathbf{r}_\mathrm{B})} - \mathcal{W}_S(\underline{\mathbf{u}}_{t'}) \Bigg], \end{aligned} \tag{A7}$$

where $\mathbf{K}_t = m_P d\mathbf{R}_t/dt$ and $\mathbf{p}_t(\mathbf{r}_\mathrm{B}) = m(\mathbf{r}_\mathrm{B}) d\mathbf{u}_t(\mathbf{r}_\mathrm{B})/dt$ are the classical projectile and crystal ion momenta, respectively, at the time t. The Jacobian factor

$$J(t) = \det \left[\frac{\partial \mathbf{R}_t \partial \underline{\mathbf{u}}_t}{\partial \mathbf{K}_o \partial \underline{\mathbf{p}}_o} \right] \tag{A8}$$

is a determinant evaluated along the classical path, which takes into account the motions of the projectile and all the crystal ions. This Jacobian factor can be related to the Maslov index [39] by expressing it as $J(t) = |J(t)| \exp(i\nu_t \pi)$, where $|J(t)|$ is the modulus of $J(t)$ and ν_t is an integer number that increases by 1 every time that $J(t)$ changes its sign along the time.

2. P-SIVR transition amplitude

By using the P-SIVR scattering state, given by Eq. (A6), within the framework of the time-dependent distorted-wave formalism [40], the P-SIVR transition amplitude reads

$$A^{(\mathrm{P-SIVR})} = -i \int_0^{+\infty} dt \, \langle \chi_f(t) | V_\mathrm{PS} \left| \Psi_i^{(\mathrm{P-SIVR})}(t) \right\rangle. \tag{A9}$$

For the evaluation of Eq. (A9) a meaningful simplification can be obtained by considering that in GIFAD the interaction time of the projectile with the crystal surface is much shorter than the characteristic time of phonon vibrations [29]. Therefore, we can assume that the crystal ions remain at their initial positions $\mathbf{u}_o(\mathbf{r}_\mathrm{B})$ during the collision, leading to

$$J(t) \approx J_P(t) = \det \left[\frac{\partial \mathbf{R}_t}{\partial \mathbf{K}_o} \right]. \tag{A10}$$

Then, by introducing the closure relation for the initial deviations of the crystal ions, the P-SIVR transition amplitude can be expressed, except for a normalization factor, as

$$\begin{aligned} A^{(\mathrm{P-SIVR})} \equiv A[a_\mathrm{if}] = & \int d\mathbf{R}_o \, f(\mathbf{R}_o) \int d\mathbf{K}_o \, g(\mathbf{K}_o) \\ & \times \int d\underline{\mathbf{u}}_o \, a_\mathrm{if}, \end{aligned} \tag{A11}$$

where

$$\begin{aligned} a_\mathrm{if} = & \int_0^{+\infty} dt \, |J_P(t)|^{1/2} e^{i\nu_t \pi/2} \, F_\mathrm{if}^{(c)}(\mathbf{R}_t, t) \\ & \times \exp\left[i(\varphi_t - \mathbf{Q} \cdot \mathbf{R}_o) \right] \end{aligned} \tag{A12}$$

is the partial amplitude associated with the classical path $\mathbf{R}_t \equiv \mathbf{R}_t(\mathbf{R}_o, \mathbf{K}_o, \underline{\mathbf{u}}_o)$, which was derived by assuming that the initial deviations $\underline{\mathbf{u}}_o$ are decoupled from $\phi_i(\underline{\mathbf{u}})$. In Eq. (A12), the function $F_\mathrm{if}^{(c)}$ is defined as

$$F_\mathrm{if}^{(c)}(\mathbf{R}_t, t) = \langle \Phi_f(t) | V_\mathrm{PS}(\mathbf{R}_t, \underline{\mathbf{u}}) | \Phi_i(t) \rangle, \tag{A13}$$

where $\Phi_j(t) = \phi_j(\underline{\mathbf{u}}) \exp(-i\epsilon_j t)$ for $j = i, f$, $\mathbf{Q} = \mathbf{K}_f - \mathbf{K}_i$, and

$$\varphi_t = \int_0^t dt' \left[\frac{(\mathbf{K}_f - \mathbf{K}_{t'})^2}{2m_P} - V_\mathrm{PS}(\mathbf{R}_{t'}, \underline{\mathbf{u}}_o) \right] \tag{A14}$$

is the SIVR phase at the time t [20]. By contrasting Eq. (A12) with the SIVR partial amplitude for a static surface, given by Eq. (6) from Ref. [3], notice that, apart from the dependence of $\mathbf{R}_t$ and φ_t on $\underline{\mathbf{u}}_o$, the P0-SIVR partial amplitude differs from the SIVR one by the substitution of the projectile-surface potential by the crystal factor $F_\mathrm{if}^{(c)}$, which is related to the first-order Born amplitude for the crystal-state transition $|\phi_i\rangle \to |\phi_f\rangle$.

3. P-SIVR differential probability

The P-SIVR differential probability for scattering with final momentum $\mathbf{K}_f$, from a crystal surface in the initial state $|\phi_i\rangle$, is obtained from Eq. (A11) as

$$\frac{dP_i^{(\mathrm{P-SIVR})}}{d\mathbf{K}_f} = \sum_{f'} |A[a_{\mathrm{if}'}]|^2, \tag{A15}$$

where the sum over f' involves the addition of all the final crystal states $|\phi_{f'}\rangle$ satisfying the total energy conservation.

In order to derive a more easy-to-handle expression for Eq. (A15), we introduce a pairwise additive model to represent the projectile-surface interaction. Within the pairwise model, $V_{\rm PS}$ is built by adding the binary interatomic potentials that describe the interaction of the atomic projectile with individual ionic centers of the crystal. It reads

$$V_{\rm PS}(\mathbf{R}_t, \underline{\mathbf{u}}) = \sum_{\mathbf{r}_{\rm B}} v_{\mathbf{r}_{\rm B}}[\mathbf{R}_t - \mathbf{r}_{\rm B} - \mathbf{u}(\mathbf{r}_{\rm B})], \tag{A16}$$

where $v_{\mathbf{r}_{\rm B}}(\mathbf{r})$ denotes the binary projectile-ion interaction as a function of the relative vector $\mathbf{r}$, with $v_{\mathbf{r}_{\rm B}} = v_1$ or v_2 to consider the two different ions of the crystallographic basis. Replacing Eq. (A16) in Eq. (A13), the crystal factor can be expressed as

$$F_{\rm if}^{(c)}(\mathbf{R}_t, t) = (2\pi)^{-3/2} \sum_{\mathbf{r}_{\rm B}} \int d\mathbf{q}\, \tilde{v}_{\mathbf{r}_{\rm B}}(\mathbf{q}) e^{i\mathbf{q}\cdot(\mathbf{R}_t - \mathbf{r}_{\rm B})} \times \langle \phi_f | \exp[-i\mathbf{q}\cdot\mathbf{U}_t(\mathbf{r}_{\rm B})] | \phi_i \rangle, \tag{A17}$$

where $\tilde{v}_{\mathbf{r}_{\rm B}}(\mathbf{q})$ is the Fourier transform of $v_{\mathbf{r}_{\rm B}}(\mathbf{r})$, and $\mathbf{U}_t(\mathbf{r}_{\rm B}) = \exp(iH_S t)\mathbf{u}(\mathbf{r}_{\rm B})\exp(-iH_S t)$ is the deviation operator within the Heisenberg picture [41].

Finally, to compare with the experiments the differential probability $dP_i^{(\rm P-SIVR)}/d\mathbf{K}_f$, given by Eq. (A15), must be averaged over the equilibrium distribution of the ϕ_i wave functions. Following a procedure similar to that given in Appendix N of Ref. [29], after some steps of algebra that involve the use of Eq. (A17), we obtain an averaged probability $dP^{(\rm P-SIVR)}/d\mathbf{K}_f$, which includes a correlation factor

$$C(\mathbf{q}, \mathbf{r}_{\rm B}, t; \mathbf{q}', \mathbf{r}'_{\rm B}, t') = \langle \exp[i\mathbf{q}'\cdot\mathbf{U}_{t'}(\mathbf{r}'_{\rm B})] \times \exp[-i\mathbf{q}\cdot\mathbf{U}_t(\mathbf{r}_{\rm B})] \rangle, \tag{A18}$$

where the averaged value $\langle X \rangle$ of any operator X, at the equilibrium temperature T, is given by Eq. (N.13) of Ref. [29]. The factor $C(\mathbf{q}, \mathbf{r}_{\rm B}, t; \mathbf{q}', \mathbf{r}'_{\rm B}, t')$ can be then expanded as a power series

$$C(\mathbf{q}, \mathbf{r}_{\rm B}, t; \mathbf{q}', \mathbf{r}'_{\rm B}, t') = \exp\left[-W_{\mathbf{r}_{\rm B}}(\mathbf{q}) - W_{\mathbf{r}'_{\rm B}}(\mathbf{q}')\right] \times \sum_{n=0}^{+\infty} c_n(\mathbf{q}, \mathbf{r}_{\rm B}, t; \mathbf{q}', \mathbf{r}'_{\rm B}, t'), \tag{A19}$$

with

$$c_n(\mathbf{q}, \mathbf{r}_{\rm B}, t; \mathbf{q}', \mathbf{r}'_{\rm B}, t') = \frac{\langle [\mathbf{q}'\cdot\mathbf{U}_{t'}(\mathbf{r}'_{\rm B})][\mathbf{q}\cdot\mathbf{U}_t(\mathbf{r}_{\rm B})]\rangle^n}{n!}, \tag{A20}$$

and $W_{\mathbf{r}_{\rm B}}(\mathbf{q})$ being the Debye-Waller function, defined as

$$W_{\mathbf{r}_{\rm B}}(\mathbf{q}) = \frac{\langle [\mathbf{q}\cdot\mathbf{u}(\mathbf{r}_{\rm B})]^2 \rangle}{2}, \tag{A21}$$

where the dependence on $\mathbf{r}_{\rm B}$ indicates that its value changes for the different species of the crystallographic basis, as well as for bulk or surface positions.

Using the expansion given by Eq. (A19), the P-SIVR probability can be expressed as a series

$$\frac{dP^{(\rm P-SIVR)}}{d\mathbf{K}_f} = \sum_{n=0}^{+\infty} \frac{dP_n}{d\mathbf{K}_f}, \tag{A22}$$

where $dP_n/d\mathbf{K}_f$ accounts for the partial probability corresponding to the $\mathbf{K}_i \to \mathbf{K}_f$ transition with the exchange of n phonons. It reads

$$\frac{dP_n}{d\mathbf{K}_f} = \sum_{\mathbf{r}_{\rm B}, \mathbf{r}'_{\rm B}} \int d\mathbf{q} \int d\mathbf{q}' \int_0^{+\infty} dt \int_0^{+\infty} dt' \times c_n(\mathbf{q}, \mathbf{r}_{\rm B}, t; \mathbf{q}', \mathbf{r}'_{\rm B}, t') \times A[b_t(\mathbf{q}, \mathbf{r}_{\rm B})]\, A[b^*_{t'}(\mathbf{q}', \mathbf{r}'_{\rm B})], \tag{A23}$$

with $A[b]$ defined by Eq. (A11) and

$$b_t(\mathbf{q}, \mathbf{r}_{\rm B}) = |J_P(t)|^{1/2} e^{i\nu_t \pi/2}\, \tilde{v}_{\mathbf{r}_{\rm B}}(\mathbf{q}) \exp\left[-W_{\mathbf{r}_{\rm B}}(\mathbf{q})\right] \times \exp\{i[\varphi_t - \mathbf{Q}\cdot\mathbf{R}_o + \mathbf{q}\cdot(\mathbf{R}_t - \mathbf{r}_{\rm B})]\}. \tag{A24}$$

From Eq. (A23) we derive more compact expressions for the orders $n = 0$ and $n = 1$, corresponding to the partial probabilities for zero- and one-phonon scattering, which are given in the text by Eqs. (1) and (2), respectively.

[1] J. Lienemann, A. Schüller, D. Blauth, J. Seifert, S. Wethekam, M. Busch, K. Maass, and H. Winter, Coherence During Scattering of Fast H Atoms from a LiF(001) Surface, Phys. Rev. Lett. **106**, 067602 (2011).

[2] J. Seifert, J. Lienemann, A. Schüller, and H. Winter, Studies on coherence and decoherence in fast atom diffraction, Nucl. Instrum. Methods Phys. Res. B **350**, 99 (2015).

[3] M. S. Gravielle and J. E. Miraglia, Influence of beam collimation on fast-atom diffraction studied via a semiquantum approach, Phys. Rev. A **92**, 062709 (2015).

[4] A. Schüller, S. Wethekam, and H. Winter, Diffraction of Fast Atomic Projectiles During Grazing Scattering from a LiF(001) Surface, Phys. Rev. Lett. **98**, 016103 (2007).

[5] P. Rousseau, H. Khemliche, A. G. Borisov, and P. Roncin, Quantum Scattering of Fast Atoms and Molecules on Surfaces, Phys. Rev. Lett. **98**, 016104 (2007).

[6] F. Aigner, N. Simonović, B. Solleder, L. Wirtz, and J. Burgdörfer, Suppression of Decoherence in Fast-Atom Diffraction at Surfaces, Phys. Rev. Lett. **101**, 253201 (2008).

[7] J. R. Manson, H. Khemliche, and P. Roncin, Theory of grazing incidence diffraction of fast atoms and molecules from surfaces, Phys. Rev. B **78**, 155408 (2008).

[8] N. Bundaleski, H. Khemliche, P. Soulisse, and P. Roncin, Grazing Incidence Diffraction of keV Helium Atoms on a Ag(110) Surface, Phys. Rev. Lett. **101**, 177601 (2008).

[9] A. Schüller, M. Busch, S. Wethekam, and H. Winter, Fast Atom Diffraction from Superstructures on a Fe(110) Surface, Phys. Rev. Lett. **102**, 017602 (2009).

[10] J. Seifert, A. Schüller, H. Winter, R. Włodarczyk, J. Sauer, and M. Sierka, Diffraction of fast atoms during grazing scattering from the surface of an ultrathin silica film on Mo(112), Phys. Rev. B **82**, 035436 (2010).

[11] P. Atkinson, M. Eddrief, V. H. Etgens, H. Khemliche, M. Debiossac, A. Momeni, M. Mulier, B. Lalmi, and P. Roncin, Dynamic Grazing Incidence Fast Atom Diffraction During Molecular Beam Epitaxial Growth of GaAs, Appl. Phys. Lett. **105**, 021602 (2014).

[12] J. Seifert and H. Winter, Young-Type Interference for Scattering of Fast Helium Atoms from an Oxygen Covered Mo(112) Surface, Phys. Rev. Lett. **108**, 065503 (2012).

[13] J. Seifert, M. Busch, E. Meyer, and H. Winter, Surface Structure of Alanine on Cu(110) Studied by Fast Atom Diffraction, Phys. Rev. Lett. **111**, 137601 (2013).

[14] A. Zugarramurdi, M. Debiossac, P. Lunca-Popa, A. J. Mayne, A. Momeni, A. G. Borisov, Z. Mu, P. Roncin, and H. Khemliche, Determination of the geometric corrugation of graphene on SiC(0001) by grazing incidence fast atom diffraction, Appl. Phys. Lett. **106**, 101902 (2015).

[15] A. Momeni, E. M. Staicu Casagrande, A. Dechaux, and H. Khemliche, Ultrafast crystallization dynamics at an organic-inorganic interface revealed in real time by grazing incidence fast atom diffraction, J. Phys. Chem. Lett. **9**, 908 (2018).

[16] A. Schüller, S. Wethekam, D. Blauth, H. Winter, F. Aigner, N. Simonović, B. Solleder, J. Burgdörfer, and L. Wirtz, Rumpling of LiF(001) surface from fast atom diffraction, Phys. Rev. A **82**, 062902 (2010).

[17] M. Debiossac, A. Zugarramurdi, Z. Mu, P. Lunca-Popa, A. J. Mayne, and P. Roncin, Helium diffraction on SiC grown graphene: Qualitative and quantitative descriptions with the hard-corrugated-wall model, Phys. Rev. B **94**, 205403 (2016).

[18] A. Schüller, D. Blauth, J. Seifert, M. Busch, H. Winter, K. Gärtner, R. Włodarczyk, J. Sauer, and M. Sierka, Fast atom diffraction during grazing scattering from a MgO(001) surface, Surf. Sci. **606**, 161 (2012).

[19] M. Debiossac, A. Zugarramurdi, H. Khemliche, P. Roncin, A. G. Borisov, A. Momeni, P. Atkinson, M. Eddrief, F. Finocchi, and V. H. Etgens, Combined experimental and theoretical study of fast atom diffraction on the $\beta_2(2\times4)$ reconstructed GaAs(001) surface, Phys. Rev. B **90**, 155308 (2014).

[20] M. S. Gravielle and J. E. Miraglia, Semiquantum approach for fast atom diffraction: Solving the rainbow divergence, Phys. Rev. A **90**, 052718 (2014).

[21] M. del Cueto, A. S. Muzas, M. F. Somers, G. J. Kroes, C. Díaz, and F. Martín, Exploring surface landscapes with molecules: Rotationally induced diffraction of H_2 on LiF(001) under fast grazing incidence conditions, Phys. Chem. Chem. Phys. **19**, 16317 (2017).

[22] P. Roncin and M. Debiossac, Elastic and inelastic diffraction of fast atoms, Debye-Waller factor, and Mössbauer-Lamb-Dicke regime, Phys. Rev. B **96**, 035415 (2017).

[23] P. Roncin, M. Debiossac, H. Oueslati, and F. Raouafi, Energy loss and inelastic diffraction of fast atoms at grazing incidence, Nucl. Instrum. Methods Phys. Res., Sect. B **427**, 100 (2018).

[24] A. Al Taleb, G. Anemone, W. W. Hayes, J. R. Manson, and D. Farías, Multiphonon excitation and quantum decoherence in neon scattering from solid surfaces, Phys. Rev. B **95**, 075414 (2017).

[25] M. C. Schram and E. J. Heller, Approach to coherent interference fringes in helium-surface scattering, Phys. Rev. A **98**, 022137 (2018).

[26] G. A. Bocan, J. D. Fuhr, and M. S. Gravielle, Van der Waals effects on grazing-incidence fast-atom diffraction for H on LiF(001), Phys. Rev. A **94**, 022711 (2016).

[27] L. Frisco, J. E. Miraglia, and M. S. Gravielle, Spot-beam effect in grazing atom-surface collisions: From quantum to classical, J. Phys.: Condens. Matter **30**, 405001 (2018).

[28] G. A. Bocan and M. S. Gravielle, GIFAD for He/KCl(001), Structure in the pattern for ⟨110⟩ incidence as a measure of the projectile-cation interaction, Nucl. Instrum. Methods Phys. Res., Sect. B **421**, 1 (2018).

[29] N. W. Ashcroft and N. D. Mermin, *Solid State Physics* (Brooks-Cole Publishing, Belmont, MA, 1976), Chap. 23.

[30] M. S. Gravielle, A. Schüller, H. Winter, and J. E. Miraglia, Fast atom diffraction for grazing scattering of Ne atoms from a LiF(001) surface, Nucl. Instrum. Methods Phys. Res., Sect. B **269**, 1208 (2011).

[31] M. S. Gravielle, J. E. Miraglia, and L. Frisco, Coherence-length effects in fast atom diffraction at grazing incidence, Atoms **6**, 64 (2018).

[32] J. E. Miraglia and M. S. Gravielle, Reexamination of the interaction of atoms with a LiF(001) surface, Phys. Rev. A **95**, 022710 (2017).

[33] H. Winter and A. Schüller, Fast atom diffraction during grazing scattering from surfaces, Prog. Surf. Sci. **86**, 169 (2011).

[34] M. Debiossac and P. Roncin, Image processing for grazing incidence fast atom diffraction, Nucl. Instr. Methods Phys. Res., Sect. B **382**, 36 (2016).

[35] A. Schüller, H. Winter, M. S. Gravielle, J. M. Pruneda, and J. E. Miraglia, He-LiF surface interaction potential from fast atom diffraction, Phys. Rev. A **80**, 062903 (2009).

[36] M. S. Gravielle and J. E. Miraglia, Single- and double-slit collimating effects on fast-atom diffraction spectra, Nucl. Instrum. Methods Phys. Res., Sect. B **382**, 42 (2016).

[37] B. Lalmi, H. Khemliche, A. Momeni, P. Soulisse, and P. Roncin, High resolution imaging of superficial mosaicity in single crystals using grazing incidence fast atom diffraction, J. Phys.: Condens. Matter **24**, 442002 (2012).

[38] W. H. Miller, The semiclassical initial value representation: A potentially practical way for adding quantum effects to classical molecular dynamics simulations, J. Phys. Chem A **105**, 2942 (2001).

[39] R. Guantes, A. S. Sanz, J. Margalef-Roig, and S. Miret-Artés, Atom-surface diffraction: A trajectory description, Surf. Sci. Rep. **53**, 199 (2004).

[40] D. P. Dewangan and J. Eichler, Charge exchange in energetic ion-atom collisions, Phys. Rep. **247**, 59 (1994).

[41] C. Cohen-Tannoudji, B. Diu, and F. Laloë, *Quantum Mechanics* (Wiley-VCH, Paris, 2011), Chap. III.